Lab on a Chip

Droplet Microfluidics for Functional Temporal Analysis and Cell Recovery on Demand using Microvalves: Application in Immunotherapies for Cancer

Journal:	*Lab on a Chip*
Manuscript ID	LC-ART-05-2022-000435.R1
Article Type:	Paper
Date Submitted by the Author:	02-Jul-2022
Complete List of Authors:	Agnihotri, Sagar; Northeastern University, Ugolini, Giovanni; Northeastern University Sullivan, Matthew; Northeastern University Yang, Yichao; Northeastern University De Ganzó, Agustín Francisco; Northeastern University Lim, Ji Won; Northeastern University Konry, Tania; Northeastern University

Droplet Microfluidics for Functional Temporal Analysis and Cell Recovery on Demand using Microvalves: Application in Immunotherapies for Cancer

Sagar N. Agnihotri, Giovanni Stefano Ugolini, *Matthew Ryan Sullivan, Yichao Yang, Augustin de Ganzo, Ji Won Lim*, *Tania Konry**

Department of Pharmaceutical Sciences, School of Pharmacy

Northeastern University, Boston, MA 02115, USA

E-mail: t.konry@northeastern.edu

Abstract

Most common methods of cellular analysis employ the top-down approach (interrogating proteomics or genomics directly), thereby destroying the cell, which does not allow the possibility of using the same cell to correlate genomics with functional assays. Herein we describe an approach for single-cell tools that serve as a bottom-up approach. Our technology allows to conduct functional phenotyping by observing cytotoxicity of cells and then probe the underlying biology. We have developed a droplet microfluidic device capable of trapping droplets in the array and release the droplet of interest selectively using microvalves. Each droplet in the array encapsulates natural killer cells (NK cells) and tumour cells for real-time monitoring of burst kinetics and spatial coordination during killing by single NK cells. Finally, we use the microvalve actuation to selectively release droplets with desired functional phenotype such as fast and serial killing of target tumour cells by NK cells. In this perspective, our device allows for interrogating first interactions and real-time monitoring of kinetics and later cell recovery on demand for single-cell omic analysis such as single-cell RNA sequencing (scRNA), which to date, is primarily based on in-depth analyses of the entire transcriptome of a relatively low number of cells.

1 Introduction

Adoptive cell transfer-based immunotherapies rely on administering highly cytotoxic immune cells, particularly T cells and natural killer (NK) cells[1,2]. Immune cells are highly heterogeneous and highly dynamic during adaptive response. It has been suggested that patients' inherent sensitivity or response to therapy is influenced by molecular heterogeneity and polymorphic characteristics of immune effector cells[2–4]. Ensuring isolation and expansion of immune cells with high anti-tumour activity presents a considerable challenge[3,5]. NK and T cells often interact with targets transiently, forming short-lived dynamic immunological synapses[6,7], which cannot be detected by end-point assays but require a dynamic, time-resolved, analytical method. It has been hypothesized that the duration of synaptic contact between immune and cancer cells is a key factor in regulating downstream effector function. In other words, the efficiency of cell regulation and later target cytotoxicity could be modified by mechanisms that enhance or decrease the intercellular *synaptic contact periods*. This necessitates functional phenotyping in a non-destructive manner to recover immune cells for downstream analysis. Current experimental paradigms either track individual cells functionally or measure genetic/protein levels of cell populations, which may not provide accurate results due to the lack of direct correlation between genetic and physiological states[8]. This severely limits our understanding of interactive and secretion dynamics from single cells and small cohorts of heterogeneous cells at single-cell resolution. Currently, there are no single-cell systems that address all of the above-described biology. However, there are various in vitro tools for single immune cell analysis available; these existing technologies have inherent limitations that affect cell retention, mobility, interactions and long-term real-time monitoring of kinetics and cell recovery on demand[9,10,19,11–18].

Droplet microfluidics has shown the ability to encapsulate single cells[20–24], hence well suited for studying single-cell interactions. Droplet microfluidic uses device geometries like T-junction[25], flow-focusing[26] and co-flow[27] to generate droplets containing cells. However, it is essential to manipulate these droplets using splitting[28–30], sorting[31–33], trapping[34–36] and merging[37,38]. Selectivity in generation[39], splitting[40], merging[41] and sorting[42] is available in the literature, but selectively releasing the trapped droplet from an array is missing to best of our knowledge. Most of the applications that involve interaction between two different kinds of cells require incubation time that may vary from 2 to 24 hours. Such applications must trap the droplet containing interacting cells for time duration and selectively release the droplet of interest. The microfluidic device with hundreds of docking sites has been demonstrated to hold

the droplet for hours[43,44]; however, the ability to selectively release the droplet of interest has not been shown. Researchers have used passive methods, active methods, and a combination of both approaches to bring selectivity in droplet manipulation. However, active methods that use electrical, thermal, and magnetic actuation can have biocompatibility issues. Use of single-layer[45,46] or multilayer valves[47,48] combined with passive methods can solve this issue.

Of note, each droplet serves as an individual bioreactor that allows cell pairs to contact each other and form immunological complexes and retains all secreted molecules that promote paracrine signalling. Our novel integrated platform has several advantages over bulk co-culture and other microfluidic approaches: (a) observations of immune cell motility, (b) quantification of single as well as serial interactions between the same cell pair; and (c) characterization of 'one-to-one' interactions between two types of cells (e.g., NK and T cells) as well as 'one-to-many' interactions, which can be studied in the same experiment by simply adjusting the initial cell density. Unlike traditional methods, we can visually identify droplets containing the precise E:T ratios of interest for analysis and can observe multiple ratios in a single chip.

While this is already of substantial interest, a breakthrough feature in the field would be to correlate functional traits with molecular signatures at single-cell resolution. This will allow us to better understand drug effects and mechanisms of action and identify genetic markers and target proteins modulating increased immune cell activity to be leveraged in future drug development. This will be possible by integrating novel technical features like a layer of pressure-actuated microvalves to the ScanDrop platform for selective collection of droplets containing the desired cells, after functional analysis, that is compatible with scRNA analyses and provides higher control on the detection parameters of immune cell activity. Thus, we will utilize a visual representation of cellular activity, such killing kinetics, interactions or various others observed via time-lapse imaging to extract droplets of interest. Unlike flow-cytometry based sorting and other methods with no visual component, we can select cells based on highly precise criteria for release and analysis. With time-lapse microscopy, we can observe a wide variety of cell behaviours that might warrant further biological analysis to uncover underlying mechanisms. With techniques such as sequencing and mass spec, -omic differences can be observed using populations only tens of cells per condition[49–52]. In immunotherapy, uncovering the biological mechanisms involved in effective versus ineffective immune cells can be utilized to greatly enhance the quality of therapy by selective cell screening or treatment to upregulate certain factors.

In this work, we designed a microfluidic device that can selectively release the droplet containing NK92 cells and K562 leukemia cell line with the help of a multilayer valve

(schematic of the workflow is shown in **figure 1**). The NK92 cell line was chosen for their high cytotoxicity and ease of culturing. K562 was chosen as a target cell due to their high susceptibility to NK cells and standard use as markers of NK cell cytotoxic potential[53–55]. The device consists of three layers: flow layer, control layer and deformable membrane. When the valve is off, droplets are trapped in the docking sites; when the valve is turned on, droplets are selectively released. For these experiments, the time required for NK cells to kill target cells was utilized as a simple but effective indicator of NK cell cytotoxic potential. The NK cells are allowed to interact with tumour cells and are imaged every 15 minutes, keeping the valve off. The NK cells that show fast killing ability are then selectively released from the docking sites with the actuation of the valve. While not in the scope of this study, the cells recollected could be subjected to single-cell sequencing or mass spectrometry to uncover the underlying physiologic producing the observed characteristics. In future, the microcontroller-based control system (e.g. Arduino) will be assembled to allow easy and user-friendly valve actuation control and scaled up design to allow a significant number of cells to be isolated. We believe that selective droplet release will allow us to uncover novel genomic and proteomic correlations to observable cell phenotypes. This will improve the biological understanding of what causes certain cell behaviours, which in turn can be utilized to improve the quality of many immune therapies.

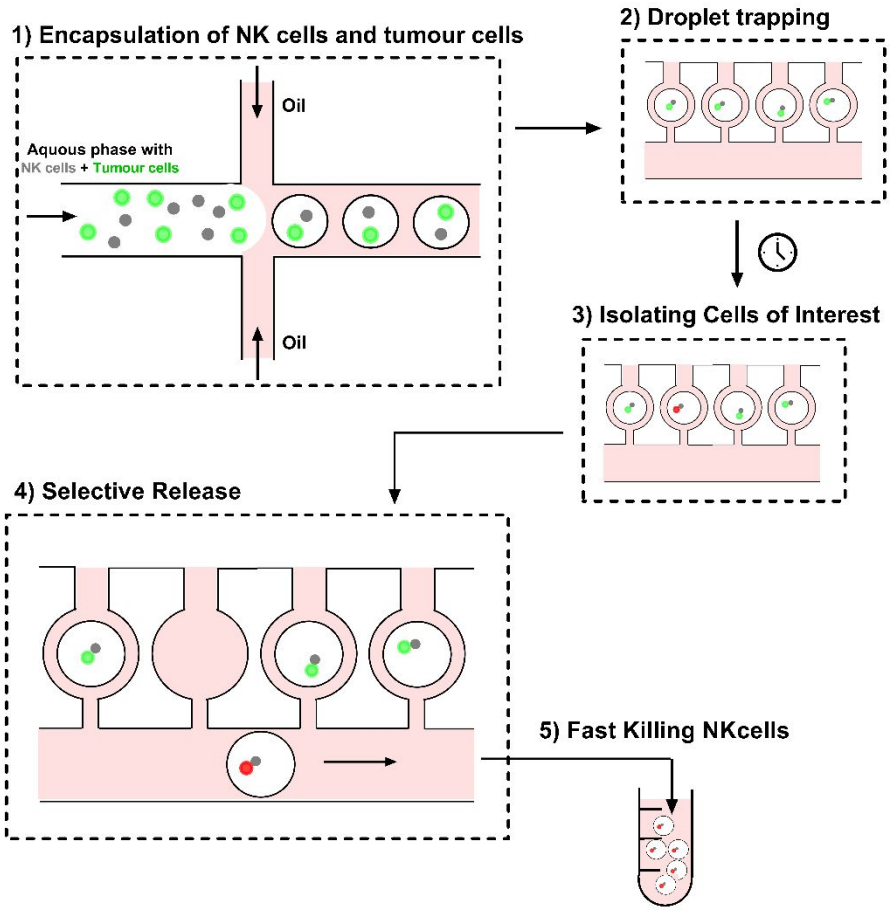

Figure 1: Schematic workflow for selective release of fast killing NK cells, consisting of 1) Generating droplets encapsulated with NK cells and tumour cells. 2) Trapping these droplets in docking sites. 3) Imaging the trapped droplets for determining the killing activity of NK cells. 4) Selectively releasing fast killing NK cells. 5) Collecting cells of interest.

2 Device design and operation

The schematic of a microfluidic device is shown in **figure 2**. The device consists of the flow layer (layer 1), control layer (layer 2), and deformable thin membrane. The flow layer consists of droplet generation and trapping section. The droplet generation section uses flow-focusing geometry; interaction between oil and aqueous phase consisting of NK cells and target cells generates droplets with a diameter ranging from 150 µm to 200 µm. The droplet trapping section consists of docking sites, and each docking site has a diameter of 200 µm. The control layer consists of valves, having four rows and twenty-three columns; the air inlets control each column. By opening or closing the extraction outlets, each valve is controlled precisely. Finally, these two layers are separated by a thin deformable membrane of 40 µm.

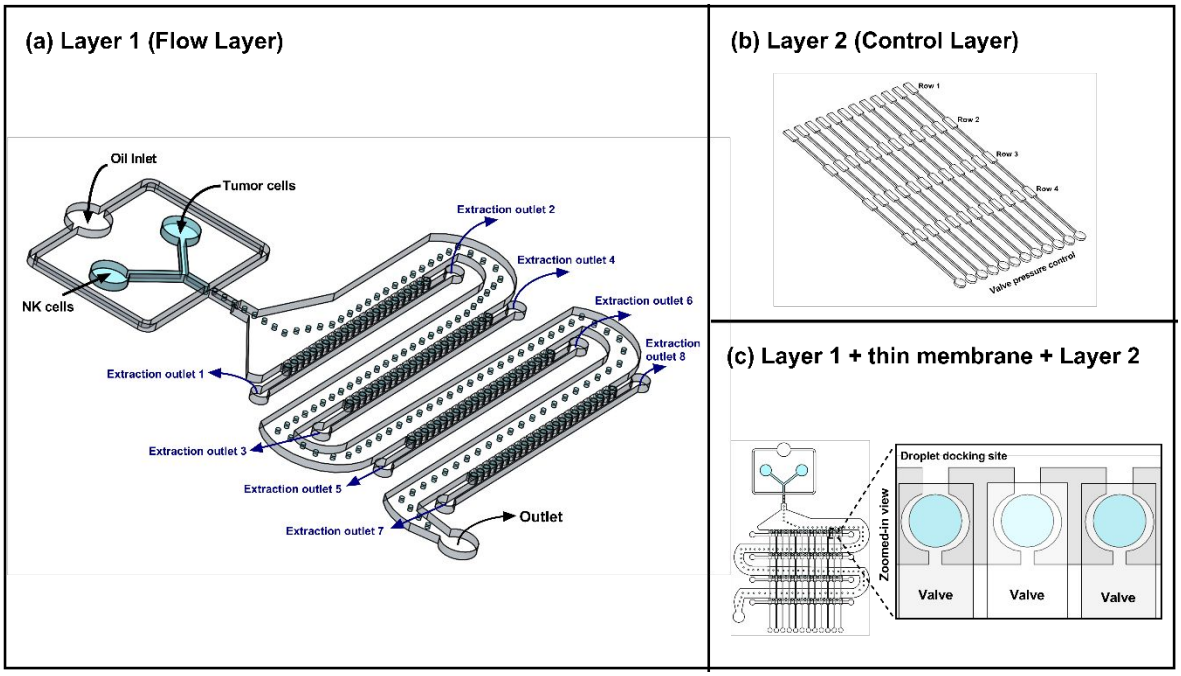

Figure 2: Schematic of the multilayered droplet microfluidic device for droplet trap and selective release of droplets **(a)** Layer 1 of the microfluidic device with a droplet generation section capable of encapsulating NK cells and Tumour cells. Moreover, the droplet trapping section consists of 4 rows, each row having two extraction outlets and capable of holding 92 droplets with the help of docking sites. **(b)** Layer 2 of the microfluidic device having microfluidic valves that can control droplet docking sites of layer 1. **(c)** Combination of layer 1, layer 2 and a deformable PDMS membrane separating them.

Figure 3 shows the overall device design, hydrodynamic resistive network, and device operation. Figure 3a shows the microscopic image of the entire device with a valve on each docking site. The trapping and releasing of droplets from each docking site are governed by the hydrodynamic resistance from the docking site to the extraction outlet. The entire microfluidic system can be considered similar to the electric resistive network, where flow rate (Q) is analogous to the current, electric resistance is analogous to the hydrodynamic resistance (R), and pressure drop (ΔP) is equivalent to the potential difference. The hydrodynamic resistance in each branch is calculated using the equation below,

$$R = \frac{12\mu l}{wh^3\left[1 - 0.63\left(h/w\right)\right]} \quad (1)$$

Where w, h, l, and μ represents the width, height, length, and viscosity of continuous phase, respectively. Figure 3b shows hydrodynamic resistance in each part of the docking site. R_{11}, R_{12} and R_{13} represent hydrodynamic resistance of entry channel, docking site and exit channel of the first docking site, respectively. The overall resistance of the first docking site is $R_1 = R_{11}$

+ R_{12} + R_{13}, similarly for the second (R_2), third (R_3), fourth (R_4) docking sites. In the same way, Q_1, Q_2, Q_3 …. represent the flow rate entering the first, second, and third docking sites. Figure 3c shows the resistive network of the half row (11 docking sites). Here we considered only half of the row because there are two extraction outlets in each row. Each half has similar hydrodynamic resistance to the other half; hence we can consider half row as symmetric to the other half. The effective resistance between the entry point of the docking site to the extraction channel is R= R_1+R_{a1}, similarly for the second docking site R= R_1+R_{a1}+R_{a2}. As effective resistance of the first docking site is always lesser than another docking site, hence flow rate entering the first docking site is always more than the other docking site ($Q_1 > Q_2 > Q_3 >$……Q_{11}).

Using the resistive network explained above, trapping and releasing a droplet can be explained. For trapping the droplet, effective resistance from the entry of the docking site to the extraction outlet is the most critical parameter. The droplet takes the path that offers the least hydrodynamic resistance. Hence, the droplet occupies/gets trapped in the first docking site with the least effective hydrodynamic resistance (R_1+R_{a1}). Once the first docking site is filled with the droplet, its resistance increases rapidly due to blocking by the droplet; hence the least resistant path for the next droplet becomes from the second docking site (R_1+R_{a1}+R_{a2}). Overall, docking sites closer to the extraction outlets get filled first with droplets, while docking sites away from the extraction outlets get filled last. Once all the docking sites are filled, droplets go to the waste outlet provided on the chip.

Similarly, for selectively releasing the trapped droplet from a docking site, it is essential to reduce the hydrodynamic resistance locally and thereby increase the flow rate (Q) entering the particular docking site. Figures 3 d and e show the valve precisely located over one of the docking sites, side view of the device when the valve is not actuated/actuated and corresponding hydrodynamic resistance. In the case of valve actuation, the thin membrane is deformed. The suction effect causes a deformation of the thin membrane, which causes a localized increase in the channel volume. The localized increase in the volume reduces the hydrodynamic resistance of the docking site. The corresponding decrease in hydrodynamic resistance is given by (R_1-R_*), where R_* is the reduction in hydrodynamic resistance due to an increase in volume. Hence effective resistance for trapping/releasing the droplet from the first docking site becomes R= (R_1-R_*) + R_{a1}. The reduction in hydrodynamic resistance causes a localized flow rate increase in the docking site, given as Q_1+Q_*, where Q_* represents an increase in flow rate.

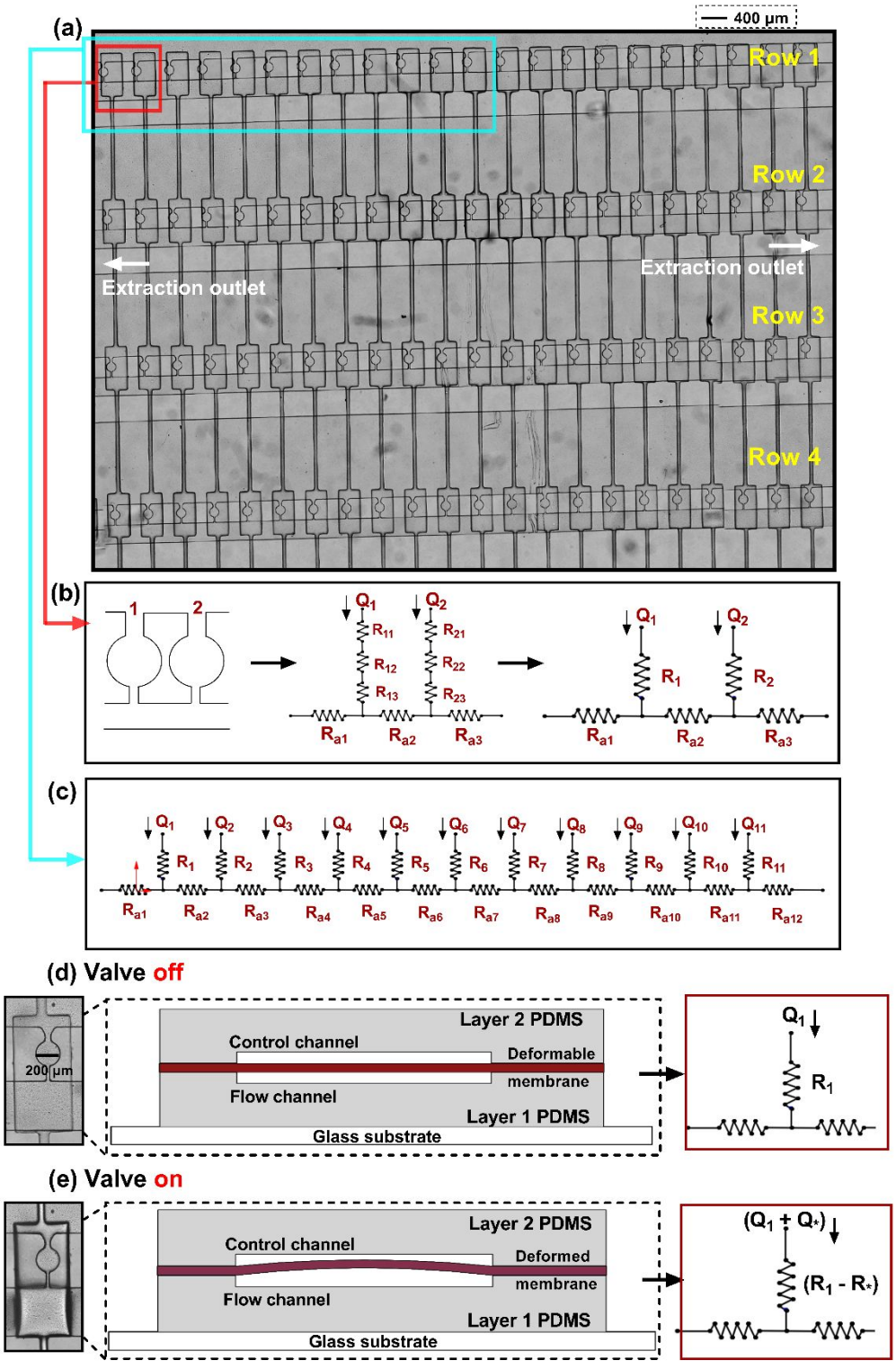

Figure 3: (a) Top view of the overall device with valves located precisely over docking site and each row having two extraction outlets. (b) The resistive network of the first two docking sites, with each branch's hydrodynamic resistance as R_{11}, R_{12} and R_{13}. The overall resistance of each docking site is represented as R_1 and R_2. (c) The resistive network of the first half of the row (11 docking sites) along with all hydrodynamic resistances and corresponding flow rates. (d) The top view of the docking site, the side view of the multilayered device, flow rate and hydrodynamic resistance when the valve is not

actuated. There is no change in the control channel and flow channel volume in this case. (e) The top view of the docking site, the side view of the device, changes in flow rate and hydrodynamic resistance when the valve is actuated. It shows a localized increase in flow channel volume caused due to deformation of the thin membrane, which reduces the resistance and increases the flow rate locally.

3 Results and Discussion

3.1 Regimes of Droplet Trap and Release without valve actuation

Once droplets are trapped in docking sites, only a continuous phase (oil) is allowed to flow, stopping the droplet generation. The continuous phase flow rate is then systematically increased from 0 to 900 µl per hour to investigate regimes of droplet trap and release without actuation of the valve. Furthermore, only extraction outlets in a row of interest and main outlet are kept open to the atmosphere while other extraction outlets are closed. We observed that under this condition, each row behaves similarly. Finally, we observed that droplets trapped in a docking site closer to the extraction outlet are easier to release with an increase in oil flow rate than the droplets trapped in docking sites away from the extraction outlet. Hence, we classified each row into three sections: section 1, section 2 and section 3, section 1 being closest to the extraction outlet on both sides while section 3 being farthest. We observed that for section 1, once the flow rate of oil exceeds 300 µl per hour, the droplet is released without actuation of the valve. Similarly, for sections 2 and 3, this value is 400 and 600 µl per hour, respectively, as shown in **figure 4**. The dotted line in **figure 4** separates the regime of droplet trap and release by plotting each section against the continuous phase flow rate. The regime map is helpful in the operation of the system. The continuous phase flow rate must be lower than 300 µl per hour to keep all the droplets in docking sites.

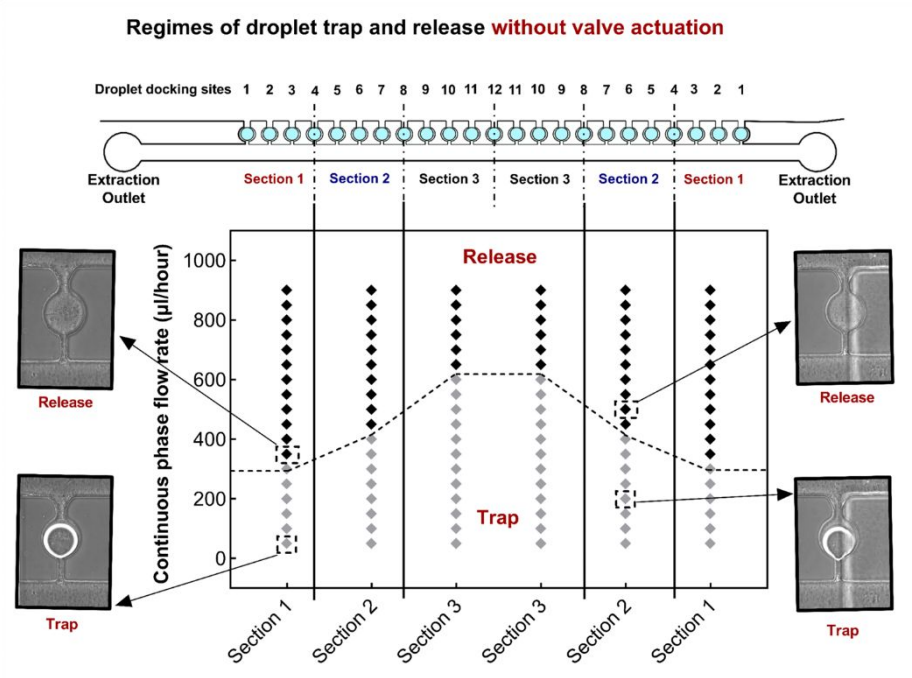

Figure 4: The regime map showing trap and release of each section against continuous phase flow rate (µl per hour). Classification of a row based on the location of docking sites is shown in the top part of the figure. The dotted line separates the regime of trap and release. Insets on the right and left sides of the figure show a visualization of a droplet trap and release in a particular section against the given flow rate of the continuous phase.

3.2 Selective Droplet Release with valve actuation

In the next step, we fully actuated the valve in the regime of trap to characterize the microfluidic system. We plotted (L_D/L_C) ratio against the time required for droplet release when the valve is actuated for each section while keeping the continuous phase flow rate constant at 250 µl/hour. L_D represents the droplet length entering a connecting exit channel, and L_C is the length of the connecting exit channel shown in **figure 5a**. The ratio of (L_D/L_C) represents a process of droplet release once the valve is actuated. The value (L_D/L_C) = 1 represents the droplet released from the docking site, and not stuck in the exit channel while the value between 0 to 1 represents the droplet still trapped in a docking site. We observed that for section 1, the droplet gets released quickly than section 2 and section 3, as shown in **figure 5b.**

After characterization of the system for droplet release, we demonstrate the selective release of a droplet from a docking site. The droplet is trapped in a docking site of section 1 in the first row to demonstrate selective droplet release. The continuous phase flow rate is kept constant at 250 µl per hour, which keeps the droplet trapped in a docking site. The image sequence of selective droplet release is shown in **figure 5c** with a scale bar. **Figure 5c** shows two droplets trapped in two adjoining docking sites. Both the docking sites have the valve

precisely placed just over it. Initially, both the valves are off, keeping droplets trapped in docking sites. When the valve on the right side is turned on, there is a localized increase in volume at the docking site, which causes the droplet to start moving in connecting channel exit, increasing the ratio of (L_D/L_C) with time shown in **figure 5d**. At 24.4 s, the droplet comes out of the docking site into a channel that connects with the extraction outlet. Later (time 28 s), the droplet moves towards the extraction outlet.

The docking site with the valve does not affect the adjoining docking site, visible in image sequences from **figure 5c.** We have also plotted (L_D/L_C) of the droplet trapped in the docking site without valve actuation in **figure 5d.** There is no change in (L_D/L_C) of the droplet trapped in the docking site without a valve actuation with time. Hence, we demonstrate the selective release of the droplet with valve actuation, proving that the valve has a very localized effect.

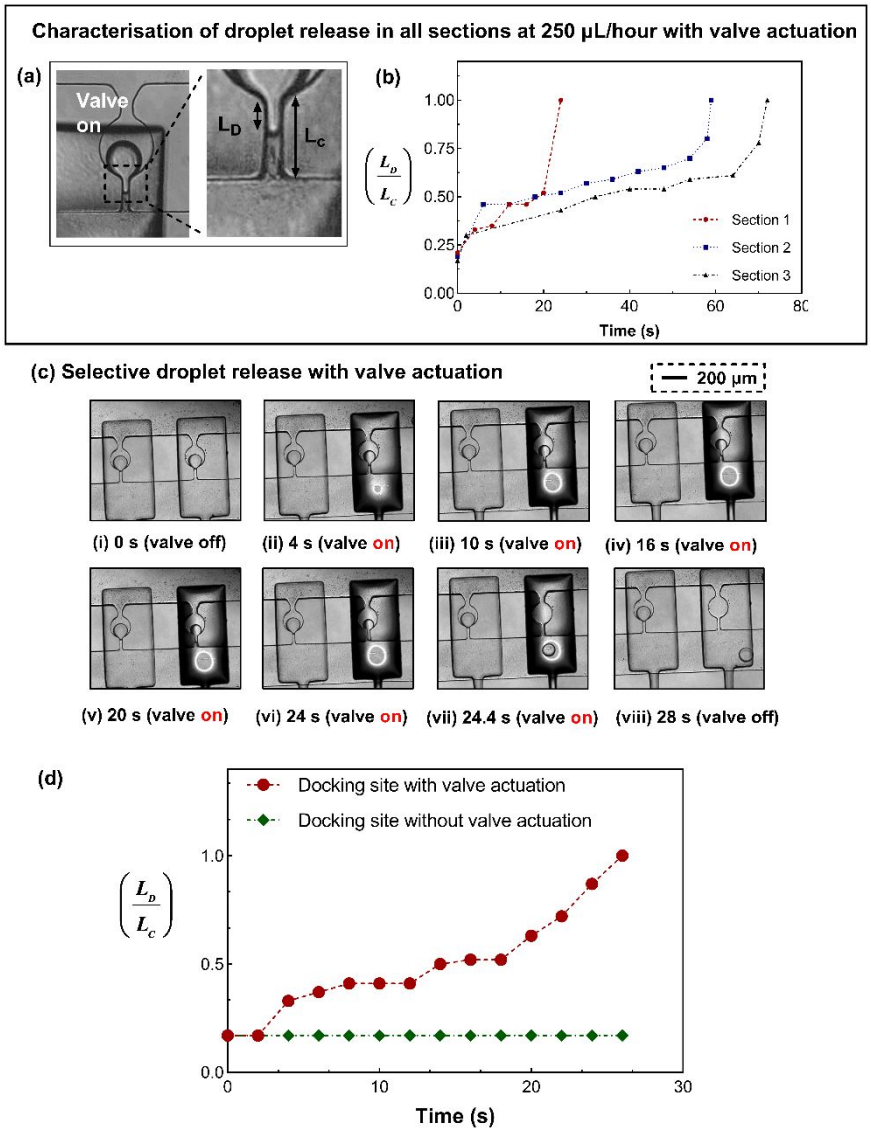

Figure 5: (a) Zoomed-in view of the docking site when the valve is actuated, showing L_D and L_C. **(b)** Characterization of the microfluidic system when the valve is fully actuated by plotting (L_D/L_C) ratio at constant (250 µl per hour) flow rate of the continuous phase plotted against the time required for release. The value of 1 represents droplet release while the ratio between 0 to 1 represents droplet still trapped. **(c)** Image sequence showing selective droplet release from a docking site. Droplet gets trapped in a docking site when the valve is off. When the valve is actuated, the droplet starts getting out of the docking site through the connecting exit channel, and finally, the droplet comes out of the docking site. The neighbouring droplet trapped in the docking site is not released, showing how the valve can have selective release. See supplementary video (S1.avi) **(d)** (L_D/L_C) of two droplets trapped in docking sites plotted against time, the first docking site is with the actuated valve, and the second docking site is without valve actuation.

3.3 Isolating Droplets with Cytotoxic NK Cells

To determine the standard kinetics for NK92 to kill K562 cancer cells on this platform, we monitored droplet co-encapsulations over the course of 15 hours. Calcein AM (green) and ethidium homodimer (red) were included to help determine target cell death. Cell deaths are discernible by an abrupt morphological change, accompanied by abrupt secretion of calcein from the cell and later an accumulation of ethidium in the nucleus. A loss of green fluorescence of ≥ 80% mean fluorescent intensity from time 0 is used to quantifiably determine cell death, confirmed by the observation of a morphological change. A total of 89 co-encapsulations were observed, and of those, 65 results in the killing of target K562 cells. Based on the average times of target cell death, we split NK cells into three groups: fast killing, average killing and slow killing (**Figure 6a**). Fast killing NK cells (20% of observed cells) were able to kill their targets within 4 hours, while slow killing NK cells (43% of observed cells) took more than 10 hours to kill or did not kill at all during the 15-hour experiment. The remaining NK (37% of observed cells) killed their targets at some point between 4 and 12 hours of co-encapsulation

Figure 6b shows an image sequence showing a droplet containing a single NK92 and K562 cell. The K562 cell is still intact and viable at 9 hours; hence, it is a slow killing NK92. Similarly, **figure 6c and 6d** shows image sequence showing killing activity of average and fast killing NK92. For average killing NK92, cell death starts at 6 hours, and before 9 hours, K562 died. A loss of green fluorescence accompanied by a morphological change of the K562, indicating cell death, is observed. In the case of fast killing NK92, cell death is observed at 3 hours, where a considerable change in fluorescence is observed compared to 0 hours, as shown in **figure 6d**. Finally, we show the serial killing ability of NK92, where one NK92 kills two or more K562 cells. **Figure 6e** shows an image sequence showing one NK92 encapsulated with two K562 cells, and both the K562 cells die at 15 hours.

Based on these criteria, we sought to identify and recollect NK cells that could kill within 4 hours or less. Shortly after this killing event was observed, the droplet was selectively released from the device, and the NK cell was recollected (**Figure 6f**). Notably, this allowed us to recollect the NK cells while it was still alive and active. This demonstrates the ability of this platform to identify effector cells of interest and quickly collect them while the cells are still intact and viable. While not necessary for single-cell downstream analytical techniques, isolation of viable cells may be valuable for subsequent analysis or expansion. For methods such as sequencing, droplets are directly collected into lysis buffer to preserve integrity of nucleic acids. To validate cell survival of the droplet selection process, we observed cell

viability for one hour after droplet isolation in the collection channel. Using calcein-AM, we confirmed the collection process did not appear to negatively impact the viability of NK92 (supplementary videos S2 and S3) or K562 (supplementary videos S3 and S4).

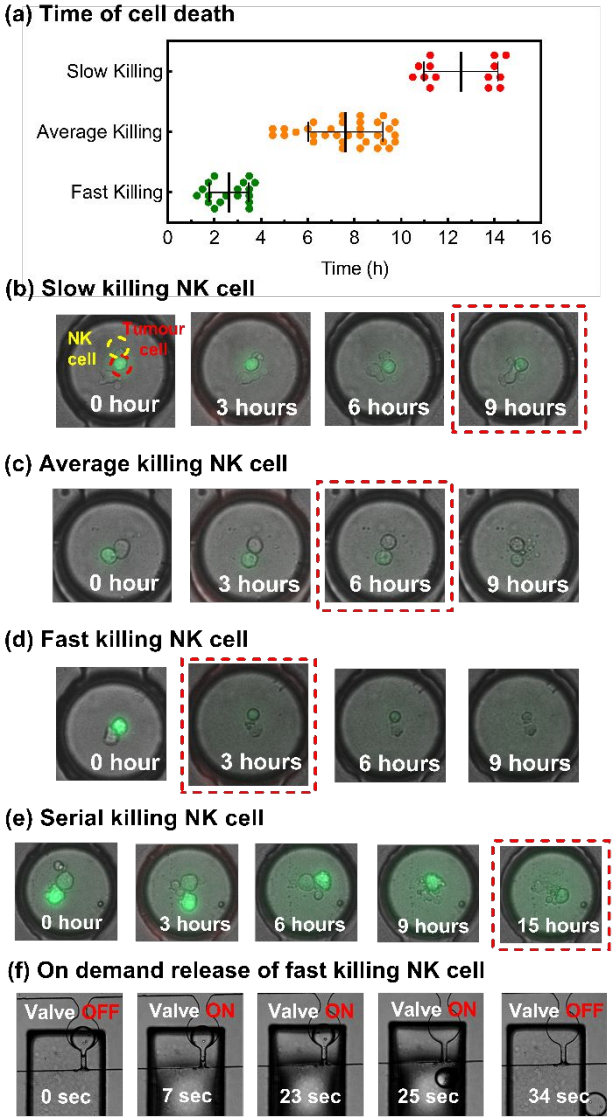

Figure 6: (a) Observed death time of individual K562 targets cells in droplets over 15 hours, divided into fast (less than 4 hours) average (4 – 12 hours) and slow (greater than 12 hours). N values are; fast killing: 18 cells, average killing: 40 cells, slow killing: 7 cells (target cells that survived the 15 hours not represented). **(b)** Image sequence displaying a single droplet containing one live slow killing NK92 and K562 cell. K562 tumour cell is labelled green, and the NK92 is unlabelled. The K562 is alive at 9 hours. **(c)** Image sequence displaying a single droplet containing one live average killing NK92 and K562 cell. The process of cell death starts after 6 hours. **(d)** Image sequence displaying a single droplet containing one live NK92 and K562 cell. K562 cell dies after 3 hours. **(e)** Image sequence displaying a single droplet containing one live NK92 and two K562 cells. Both the cells die at 15 hours. **(f)** Image sequence displaying the selective release of the droplet of interest (fast killing NK cell) shortly after target cell death.

4 Conclusions

In the present work, we have developed a droplet-based microfluidic platform with integrated multilayer microvalves to trap and selectively release a droplet of interest encapsulated with NK cells and tumour cells. The main aim of the present work is to design a biocompatible method for selectively releasing droplets of interest from an array of droplets. A flow-focusing device generates water-in-oil droplets, and the aqueous phase consists of NK cells and tumour cells. These generated droplets are then allowed to get trapped in 92 docking sites. The microvalves in a different layer are precisely placed over a docking site; a deformable PDMS membrane separates these layers. A cytotoxicity-based experiment was chosen for our proof of concept for identifying and collecting immune cells with unique phenotypic properties. Over 3-4 hours, we visualize each docking site to identify a droplet containing fast killing NK cells from an array of droplets and collected them in one of the extraction outlets. The biocompatibility of the present system makes it an ideal candidate for single-cell analysis, drug screening and interdisciplinary research applications. Upon observing a particular event, the ability to immediately release droplets of interest allows for recollection of viable effector cells, which is essential for certain types of downstream analysis such as transcriptomic sequencing. The present microfluidic system can trap and release a droplet from an array of droplets, and with further improvement, even thousands of droplets can be trapped and selectively released. This same system may be applied to a wide range of different phenotypic markers of interest, including motility, calcium signalling, serial killing, viability, secretions and other observable features. A more precise correlation between -omics of immune cells and the various phenotypes observed is an important step towards understanding the factors that contribute to successful immunotherapy. In future, the microcontroller-based control system and scaled up design will allow a significant number of cells to be isolated.

5 Methods and Materials

5.1 Device fabrication

The microfluidic device's flow channel (layer 1) and control channel (layer 2) was fabricated using standard soft lithography. The photomasks required for the flow channel and control channel were drawn in AutoCAD. Negative photoresist SU8 is spin-coated on a 4-inch silicon wafer and subjected to UV light for preparing the master mould. Polydimethylsiloxane (PDMS) and curing agent in a ratio of (10:1) were mixed and poured on the master mould of both layers

to prepare a replica of PDMS. The thin deformable PDMS membrane is prepared by spin coating PDMS + curing agent (10:1) at 1000 rpm for 2 minutes. Finally, all three layers were assembled: The control layer was punched for air inlet and bonded to PDMS membrane by subjecting it to air plasma (Harrick Plasma). The control layer and PDMS membrane are bonded with the flow channel by precisely aligning valves over docking sites under the microscope. This entire assembly was then bonded to a glass slide. One-hour baking follows each bonding process in a convection oven at 70 ^{0}C.

5.2 Cell Culture

NK92 cells and K562 human leukemia cells were acquired from ATCC. NK-92 were cultured using X-VIVO10 media (Lonza) supplemented with 10% heat-inactivated FBS (Gibco) and 500 IU/mL IL2 (Prospec). K562 were cultured in RPMI1640 media supplemented with 10% heat-inactivated FBS and 1% antibiotic-antimycotic mixture (Gibco). Cell medias were combined at a 1:1 ratio for droplet co-encapsulations. Cells were kept at 37°C and 5% CO_2. Both NK92 cells and K562 human leukaemia cells were used in a concentration of 3×10^6 cells/mL.

5.3 Droplet Generation

The water-in-oil droplets were generated upstream using a flow-focusing junction. The aqueous phase consisted of NK cells and tumour cells mixed before reaching a flow-focusing junction at 250 µl per hour, as shown in **figure 2**. FC-40 with 2% surfactant Span-80 was used as a continuous phase at 1000 µl per hour. The oil and aqueous phase were pumped in a microfluidic device using three syringe pumps. Under the flow-focusing geometry dimensions, droplets having a diameter in the range of 150 to 200 µm were generated. These generated droplets were trapped in docking sites; all the outlets are kept open during this process. Once all the docking sites are filled, aqueous phase flow is stopped, while oil is allowed to flow, resulting in no droplet generation. The droplets encapsulating NK cells and tumour cells trapped in a docking site were incubated at 37 ^{0}C in a microscope chamber for imaging live experiments to observe the killing activity of NK cells.

5.4 Microscopy

Devices images and data were acquired using a Zeiss Axio Observer.Z1 with Hamamatsu C10600 Orca-R2 digital camera. Fluorescence was observed using standard FITC and dsRed filters. The microscope is equipped with an incubated stage to maintain cells at 37°C and 5% CO_2 during experiments. Target cell killing was observed at 20X magnification every 15 minutes over the course of 15 hours. Results were analyzed using Zen Blue software (Zeiss). Droplet releasing was recorded at 5X magnification using bright field imaging. Images of the entire device array were taken at 10X magnification and processed using the Zen Blue stitching feature.

Contributions:

SNA, GSU ,MRS and YY contributed equally.

Acknowledgement

This study was funded by National Institute of Health grants R33 (1R33CA223908-01) and R01 (5R01GM127714-04), National Science Foundation (CBET-1803872) grant awarded to Dr Tania Konry.

References

1 M. W. Rohaan, S. Wilgenhof and J. B. A. G. Haanen, *Virchows Arch.*, 2019, **474**, 449–461.

2 L. Zhang, M. Liu, S. Yang, J. Wang, X. Feng and Z. Han, *Am. J. Cancer Res.*, 2021, **11**, 1770–1791.

3 H. E. Ghoneim, A. E. Zamora, P. G. Thomas and B. A. Youngblood, *Trends Mol. Med.*, 2016, **22**, 1000–1011.

4 D. Di, P. Oberoi, K. Kamenjarin, J. Francisco, V. Ossa, B. Uherek, H. Bönig and W. S. Wels, *Cells*, 2020, **9**, 1–20.

5 M. Granzin, J. Wagner, U. Köhl, A. Cerwenka, V. Huppert and E. Ullrich, *Front. Immunol.*, , DOI:10.3389/fimmu.2017.00458.

6 Emily M. Mace and Jordan S. Orange, *Immunobiology*, 2011, **118**, 2363–2364.

7 J. Xie, C. M. Tato and M. M. Davis, *Immunol. Rev.*, 2013, **251**, 65–79.

8 S. Darmanis, C. J. Gallant, V. D. Marinescu, M. Niklasson, A. Segerman, G. Flamourakis, S. Fredriksson, E. Assarsson, M. Lundberg, S. Nelander, B. Westermark and U. Landegren, *Cell Rep.*, 2016, **14**, 380–389.

9 K. Guldevall, B. Vanherberghen, T. Frisk, J. Hurtig, A. E. Christakou, O. Manneberg, S. Lindström, H. Andersson-Svahn, M. Wiklund and B. Önfelt, *PLoS One*, , DOI:10.1371/journal.pone.0015453.

10 Y. J. Yamanaka, C. T. Berger, M. Sips, P. C. Cheney, G. Alter and J. C. Love, *Integr. Biol. (United Kingdom)*, 2012, **4**, 1175–1184.

11 P. J. Lee, P. J. Hung, R. Shaw, L. Jan and L. P. Lee, *Appl. Phys. Lett.*, 2005, **86**, 1–3.

12 A. M. Skelley, O. Kirak, H. Suh, R. Jaenisch and J. Voldman, *Nat. Methods*, 2009, **6**, 147–152.

13 B. Dura, Y. Liu and J. Voldman, *Lab Chip*, 2014, **14**, 2783–2790.

14 S. Faley, K. Seale, J. Hughey, D. K. Schaffer, S. Vancompernolle, B. McKinney, F. Baudenbacher, D. Unutmaz and J. P. Wikswo, *Lab Chip*, 2008, **8**, 1700–1712.

15 J. P. Frimat, M. Becker, Y. Y. Chiang, U. Marggraf, D. Janasek, J. G. Hengstler, J. Franzke and J. West, *Lab Chip*, 2011, **11**, 231–237.

16 T. P. Lagus and J. F. Edd, *J. Phys. D. Appl. Phys.*, , DOI:10.1088/0022-3727/46/11/114005.

17 I. K. Dimov, R. Lu, E. P. Lee, J. Seita, D. Sahoo, S. M. Park, I. L. Weissman and L. P. Lee, *Nat. Commun.*, , DOI:10.1038/ncomms4451.

18 B. Dura, S. K. Dougan, M. Barisa, M. M. Hoehl, C. T. Lo, H. L. Ploegh and J. Voldman, *Nat. Commun.*, , DOI:10.1038/ncomms6940.

19 K. Chung, C. A. Rivet, M. L. Kemp and H. Lu, *Anal. Chem.*, 2011, **83**, 7044–7052.

20 H. Yin and D. Marshall, *Curr. Opin. Biotechnol.*, 2012, **23**, 110–119.

21 A. E. Sgro, P. B. Allen and D. T. Chiu, *Anal. Chem.*, 2007, **79**, 4845–4851.

22 E. X. Ng, M. A. Miller, T. Jing and C. H. Chen, *Biosens. Bioelectron.*, 2016, **81**, 408–414.

23 T. Konry, S. Sarkar, P. Sabhachandani and N. Cohen, *Annu. Rev. Biomed. Eng.*, 2016,

18, 259–284.

24 M. R. Raveshi, M. S. Abdul Halim, S. N. Agnihotri, M. K. O'Bryan, A. Neild and R. Nosrati, *Nat. Commun.*, , DOI:10.1038/s41467-021-23773-x.

25 P. Garstecki, M. J. Fuerstman, H. A. Stone and G. M. Whitesides, *Lab Chip*, 2006, **6**, 437–446.

26 S. L. Anna, N. Bontoux and H. A. Stone, *Appl. Phys. Lett.*, 2003, **82**, 364–366.

27 C. Cramer, P. Fischer and E. J. Windhab, *Chem. Eng. Sci.*, 2004, **59**, 3045–3058.

28 D. R. Link, S. L. Anna, D. A. Weitz and H. A. Stone, *Phys. Rev. Lett.*, 2004, **92**, 054503.

29 L. Ménétrier-Deremble and P. Tabeling, *Phys. Rev. E*, 2006, **74**, 035303(R).

30 Z. Che, N. T. Nguyen and T. N. Wong, *Appl. Phys. Lett.*, 2011, **98**, 2009–2012.

31 L. Xu, H. Lee, R. Panchapakesan and K. W. Oh, *Lab Chip*, 2012, **12**, 3936.

32 H. D. Xi, H. Zheng, W. Guo, A. M. Gañán-Calvo, Y. Ai, C. W. Tsao, J. Zhou, W. Li, Y. Huang, N. T. Nguyen and S. H. Tan, *Lab Chip*, 2017, **17**, 751–771.

33 A. R. Abate, J. J. Agresti and D. A. Weitz, *Appl. Phys. Lett.*, , DOI:10.1063/1.3431281.

34 A. Huebner, D. Bratton, G. Whyte, M. Yang, A. J. Demello, C. Abell and F. Hollfelder, *Lab Chip*, 2009, **9**, 692–698.

35 W. Wang, C. Yang and C. M. Li, *Lab Chip*, 2009, **9**, 1504–1506.

36 W. Wang, C. Yang, Y. Liu and C. M. Li, *Lab Chip*, 2010, **10**, 559–562.

37 X. Niu, S. Gulati, J. B. Edel and A. J. Demello, *Lab Chip*, 2008, **8**, 1837–1841.

38 X. Chen, A. Brukson and C. L. Ren, *Microfluid. Nanofluidics*, 2017, **21**, 1–10.

39 D. J. Collins, T. Alan, K. Helmerson and A. Neild, *Lab Chip*, 2013, **13**, 3225–3231.

40 M. R. Raveshi, S. N. Agnihotri, M. Sesen, R. Bhardwaj and A. Neild, *Sensors Actuators B. Chem.*, 2019, **292**, 233–240.

41 S. N. Agnihotri, M. R. Raveshi, R. Bhardwaj and A. Neild, *Microfluid. Nanofluidics*, 2021, **25**, 1–13.

42 C. N. Baroud, J. P. Delville, F. Gallaire and R. Wunenburger, *Phys. Rev. E - Stat. Nonlinear, Soft Matter Phys.*, 2007, **75**, 1–5.

43 S. Sarkar, P. Sabhachandani, D. Stroopinsky, K. Palmer, N. Cohen, J. Rosenblatt, D. Avigan and T. Konry, *Biomicrofluidics*, 2016, **10**, 1–12.

44 S. Sarkar, N. Cohen, P. Sabhachandani and T. Konry, *Lab Chip*, 2015, **15**, 4441–4450.

45 S. N. Agnihotri, M. R. Raveshi, R. Bhardwaj and A. Neild, *Langmuir*, 2020, **36**, 1138–1146.

46 S. N. Agnihotri, M. R. Raveshi, R. Bhardwaj and A. Neild, *Phys. Rev. Appl.*, 2019, **11**, 034020.

47 M. A. Unger, H. P. Chou, T. Thorsen, A. Scherer and S. R. Quake, *Science (80-.).*, 2000, **288**, 113–116.

48 H. W. Zhu, N. G. Zhang, R. X. He, S. Z. Li, S. S. Guo, W. Liu and X. Z. Zhao, *Microfluid. Nanofluidics*, 2011, **10**, 1343–1349.

49 G. D. Evrony, A. G. Hinch and C. Luo, *Annu. Rev. Genomics Hum. Genet.*, 2021, **22**, 171–197.

50 A. Kulkarni, A. G. Anderson, D. P. Merullo and G. Konopka, *Curr. Opin. Biotechnol.*, 2019, **58**, 129–136.

51 L. M. Hu R, Li Y, Yang Y, *Mass Spectrom Rev.*

52 P. Hu, W. Zhang, H. Xin and G. Deng, *Front. Cell Dev. Biol.*, 2016, **4**, 1–12.

53 J. E. Nagel, G. D. Collins and W. H. Adler, *Cancer Res.*, 1981, **41**, 2284–2288.

54 X. Song, C. Xu, X. Wu, X. Zhao, J. Fan and S. Meng, *Biologicals*, 2020, **68**, 46–53.

55 S. Neri, E. Mariani, A. Meneghetti, L. Cattini and A. Facchini, *Clin. Diagn. Lab. Immunol.*, 2001, **8**, 1131–1135.